Microwave-assisted synthesis of platelet-like cobalt metal-organic framework, its transformation to porous layered cobalt-carbon nanocomposite discs and their utilization as anode materials in sodium-ion batteries

David Skoda [a*], Tomas Kazda [b], Lukas Munster [a], Barbora Hanulikova [a], Ales Styskalik [c], Pierre Eloy [c], Damien P. Debecker [c], Jarmila Vilcakova [a], Ondrej Cech [b], Lucie Simonikova [d], Viktor Kanicky [d], and Ivo Kuritka [a]

[a] Centre of Polymer Systems, Tomas Bata University in Zlin, Tr. Tomase Bati 5678, Zlin, CZ-76001, Czech Republic

[b] Department of Electrical and Electronic Technology, Faculty of Electrical Engineering and Communication, Brno University of Technology, Technicka 10, Brno, CZ-616 00, Czech Republic

[c] Institute of Condensed Matter and Nanoscience, UCLouvain, Place Louis Pasteur, 1, 1348 Louvain-La-Neuve, Belgium

[d] Department of Chemistry, Faculty of Science, Masaryk University, Kotlarska 2, CZ-61137 Brno, Czech Republic

Abstract

In this work a facile microwave-assisted synthesis of a platelet-like cobalt-based metal-organic framework (MOF) material is presented. This material was synthesized from cobalt(II) acetylacetonate and biphenyl-4,4′-dicarboxylic acid (Bpdc) in N,N'-dimethylformamide at 160 °C. As-prepared Co-Bpdc MOF product with a platelet-like disc architecture was transformed by heat treatment in a nitrogen atmosphere at 800 °C to porous cobalt-carbon nanocomposite discs. It is demonstrated that this synthetic strategy allows for obtaining magnetic microporous carbon layered discs with homogeneously incorporated metallic cobalt nanoparticles with a size of ca. 4 nm. The Co-C nanocomposite material was characterized by a variety of physico-chemical methods. It is shown that both Co-Bpdc MOF and Co-C nanocomposite were electrochemically active in sodium battery system as a material for the

* Corresponding author. E-mail: dskoda@utb.cz

negative electrode. The high capacity retention over 80% and capacities over 200 mAh g^{-1} in the sodium-ion battery systems have been achieved.

1 Introduction

Sodium-ion batteries (NIBs) are nowadays considered as the next generation post-lithium power sources [1]. NIBs have several advantages, mainly linked to large scale energy storage and conversion due to the high abundance and the low cost of sodium compared to lithium. Thus, sodium-ion batteries are considered as a promising post-lithium system. However, there are still some limitations addressed to NIBs such as relatively lower ionization potential of Na^+ ion in comparison to Lithium-ion batteries (LIBs) and also a bigger diameter of Na^+ ions which confines the diffusion. Moreover, bigger diameter of Na^+ ion leads to decomposition of the structure of graphite anodes used in Li-ion batteries. Therefore, graphite as anode for Na-ion batteries is inapplicable and it is necessary to find a new stable anode material [2]. These issues lead to lower energy density and poor electrochemical performance in comparison with LIBs [3]. To overcome these drawbacks, many strategies involving nanosizing and preparation of composite materials were applied as promising solutions how to improve NIBs performance [3]. Nevertheless, the research, development, and application of new composite electrode materials suitable for sodium-ion batteries are still in their infancy.

Carbon-based composite materials have attracted immense research interest due to their high surface area, and thermal, mechanical, electronic, catalytic, and optical properties [4,5]. Since these materials provide interesting electrochemical properties, increased effort is focused on their application in electrochemical power sources [6–8]. It has also been reported that carbon-based materials can be utilized as negative electrode materials in sodium-ion batteries (NIBs) [1,3,9]. However, it is worth mentioning that graphite and other carbon-based materials with high graphitization exhibit unfeasible capacity (less than 100 mA h g^{-1}) for Na^+ storage [10]. For this reason, ongoing research has focused on disordered soft and hard carbon-based materials which exhibit high reversible capacity during the long-term cycling, however, they suffer from high irreversible capacity in the first cycles [11–14]. It has already been shown that composites of cobalt and carbon possess interesting electrochemical properties and therefore attract considerable interest in energy storage applications. Such example is found in the work by Wu et al., where Co-carbon nanowire derived carbon-encapsulated cobalt chalcogenide nanowires were investigated as an efficient anode material for NIBs [15]. Although there are

many types of cobalt containing carbon nanocomposite materials [15–19] based on carbon nanotubes, graphene sheets, porous carbon, etc., the preparation of homogeneous nanocomposite materials via fast and low-cost methods still remains a challenge. Considering the possible application in energy storage, the homogeneity of cobalt-carbon composites presents the decisive property of the final material. It was found recently that the decomposition of metal-organic frameworks (MOFs) represents a very effective way for the preparation of homogeneous carbon-based composites [20–22].

MOFs are classified as porous crystalline solids constructed from metal ions or metal-oxo clusters crosslinked with an organic linker [23]. The diversity of carbon-containing linkers with adjustable size, connectivity, and functional groups brings a possibility to tune the final properties of MOF materials such as composition, design, architecture, porosity, and electrochemical properties [24–30]. MOFs are usually prepared via a solvothermal reaction of a metal salt or metal-oxo clusters with carboxylate linkers in N,N'-dimethylformamide [25,31]. It is worth noting that microwave-assisted (MW) methods have attracted considerable attention in the field of MOF preparation, because they allow for a significant enhancement of the reaction rates and the ability to control the phase and size of products [32–34]. It is worth mentioning that hydrothermal syntheses of cobalt-based MOF materials with biphenyldicarboxylate linkers were reported by Rueff et al. [35] and Pan et al. [36]. Furthermore, the syntheses and applications of Co-MOF materials containing naphthalenedicarboxylate linkers have been recently reviewed by Gangu et al. [37].

It should be taken into account that MOFs were reported as efficient materials for batteries [38–41]. Compared to sodium salts investigated as NIBs anode materials, such as Na_2TP (disodium terephthalate) and its derivatives, MOFs possess several beneficial features when applying them in NIBs: (i) ionization energy (IE) of transition metal ions in MOFs is higher than IE of sodium ions in sodium organic salts resulting in better stability in organic electrolytes; (ii) stable coordination network between transition metal centers and organic linkers also possibly restricts its dissolution in electrolytes. For example, the sodium ion batteries with Co-MOF/rGO hybrid material anode reported by Dong reached the capacity of 206 mAh g^{-1} after 330 cycles at 500 mA g^{-1} [40]. Pan and coworkers reported an aqueous preparation of Co-bpdc MOF based on a linear ligand (biphenyl-4,4′-dicarboxylic acid) [36]. This Co-bpdc material was recently investigated by Zhang and coworkers as a novel anode material with high Na^+ storage performance (269 mA h g^{-1} at 20 mA g^{-1}) and capacity retention (79.0 % after 1000 cycles at

100 mA g^{-1}) [42]. Notably, phenyl-containing molecules were found to be favorable for Na^+ diffusion [43].

Well defined stoichiometry and homogeneous structure of MOF materials allow for obtaining highly homogeneous carbon-based composite materials upon thermal treatment of MOFs in non-oxidizing atmosphere [44,45]. For instance, the synthesis of mixed metal/metal oxide-carbon nanoporous materials through a direct carbonization of binary mixed-MOF (CoMn-MOF-74) synthesized from 2,5-dihydroxyterephthalic acid was reported by Wang et al. [46]. Recently, several papers have described the nanocomposites of cobalt embedded in various carbon structures derived from ZIF-67 metal-organic frameworks containing 2-methylimidazole linkers [22,47–49]. Based on the survey mentioned above, MOFs can be considered as attractive precursors for carbon based composite materials. In addition to that, the utilization of MOF-derived materials for sodium energy storage was recently reviewed by Zou et al. and Ingersoll et al. [50,51].

Herein we introduce a facile strategy for the preparation of layered cobalt metal-organic framework and its further transformation to metallic cobalt nanoparticles (size of ca. 4 nm) dispersed in a porous carbon matrix. Our approach is based on application of layered biphenyl-4,4'-dicarboxylate based cobalt metal-organic framework (Co-Bpdc) synthesized via non-aqueous microwave-assisted synthesis as a single source precursor for Co-carbon based material. Preformed Co-Bpdc precursor with layered architecture contains Co^{2+} ions crosslinked by oxygen-containing dicarboxylic acid linker (Bpdc) and therefore it acts as a source of both cobalt and carbon. It is worth noting that no inert atmosphere is required within the synthesis of Co-Bpdc. Moreover, the Co-Bpdc precursor is easily transformed - via thermal treatment in an inert atmosphere (N_2) at the temperature of 800 °C - into porous layered composite discs featuring homogeneously dispersed metallic cobalt nanoparticles in a carbon matrix (labeled as Co-C). The structural and electrochemical properties of Co-Bpdc and Co-C products were studied by various physical-chemical methods such as infrared and Raman spectroscopies, powder X-Ray diffraction, electron microscopy, thermogravimetry, and X-Ray photoelectron spectroscopy. Both, the obtained Co-Bpdc MOF and Co-C nanocomposite discs were tested as anode materials in sodium-ion batteries by means of cyclic voltammetry and galvanostatic cycling at different C-rates. The NIBs with the Co-Bpdc and Co-C anode materials exhibited promising performance.

2 Experimental

2.1 Chemicals

Biphenyl-4,4′-dicarboxylic acid (H_2bpdc, 97 %, M_w = 242.23 g mol^{-1}) and cobalt(II) acetylacetonate Co(II)$(Acac)_2$ (99 %, M_w = 257.15 g mol^{-1}) were supplied from Sigma Aldrich. N,N′-dimethylformamide DMF (p.a.) and chloroform (p.a.) were purchased from Penta (Czech Republic). Chemicals for Na-ion cells fabrication such as sodium perchlorate ($NaClO_4$), poly(vinylidenefluoride) (PVDF), N-methyl-2-pyrrolidone (NMP), ethylene carbonate (EC), dimethyl carbonate (DMC) and carbon Super P (TIMCAL) were supplied from Sigma Aldrich and TIMCAL Graphite & Carbon.

2.2 Synthesis

The typical synthesis of Co-Bpdc material in a microwave reactor was as follows: Co(II)$(acac)_2$ (0.393 g, 1.53 mmol) was dissolved in 60 ml of N,N'-dimethylformamide (DMF) in a Teflon container under ambient atmosphere. After the dissolution of the cobalt precursor, biphenyl-4,4′-dicarboxylic acid (0.498 g, 2.06 mmol) was added and the container was tightly closed and placed into a microwave reactor. Reaction mixture was heated up to 160 °C under microwave irradiation in 2 cycles while the duration of each cycle was 20 min with a pause of 5 minutes between them. Microwave power was set to 50 % (300 W). The reaction was stopped after 45 minutes. Microwave reactor record is illustrated in Supplementary materials (Figure 1S). Once the reaction mixture was cooled to 50 °C, the reactor was removed and the resulting violet precipitate was filtered on a Büchner funnel and finally washed with chloroform. The violet powder product was dried at 90 °C in an oven and weighed. Yield of Co-Bpdc product: 0.307 g (59 % based on formula estimated from TG/DSC analysis, see discussion).

To release volatile byproducts and residual solvent from the sample and to further apply this material in NIB cell, as-prepared Co-Bpdc was heated for 1 hour at 340 °C (heating ramp 5 °C min^{-1}) in an atmosphere of air. This sample was labeled as Co-Bpdc-340. To produce cobalt-carbon based nanocomposite, Co-Bpdc material was heated in N_2 atmosphere up to 800 °C starting at room temperature with a 5 °C min^{-1} heating ramp and then held at 800 °C for 1 h. Obtained product is labeled as Co-C sample.

The analysis of as-prepared powder product Co-Bpdc:

FTIR (ATR, diamond crystal, cm^{-1}) ν: 418 w, 454 s (Co-O), 485 w, 527 vw (ring out-of-plane), 597 vw, 678 s (ring out-of-plane), 698 w (ring out-of-plane), 746 m, 767 vs (δ CH, bending), 795 vw, 842 w (ν NC), 878 vw, 1005 w (ν CC/δ CH), 1109 w (δ CH_3/CO), 1132 vw, 1177 w

(δ CH_3), 1254 w (ν CC), 1339 s, 1381 vs (ν_{sym} COO), 1445 w, 1514 w (ν CN), 1547 m (ν_{asym} COO), 1589 m (ν_{asym} COO), 1605 m (ν_{asym} COO), 1651 m (ν C=O), 2931 vw (ν CH_3), 3311 vw (ν OH).

Elemental analysis (ICP-OES): 16.0 ± 0.1 wt% Co.

2.3 Electrochemical analysis and electrode preparation

A mixture consisting of Co-Bpdc-340 or Co-C sample, PVDF (polyvinylidene fluoride) (binder) and Super P carbon was mixed by a magnetic stirrer in a vial with 1 ml NMP (N-methyl-2-pyrrolidone) in the weight ratio as follows: active material 80 %, Super P 10 %, PVDF 10 %. The resulting mixture was deposited on an Al foil by a 200 µm coating bar, dried at 60 °C under ambient atmosphere and, after the solvent was evaporated, pressed by the pressure of 29420 kN m^{-2}. The discs with the diameter of 18 mm were cut out from the coated Al foil and subsequently dried at 110 °C under the vacuum. The discs were finally inserted into an electrochemical cell El-Cell© ECC-Std and assembled in argon atmosphere inside a Jacomex glove box with less than 1 ppm of oxygen and water content. A sodium metal disc was used as the anode and 1 mol l^{-1} $NaClO_4$ in EC (ethylene carbonate):DMC (dimethyl carbonate) in the ratio 1:1 w/w as the electrolyte. The electrolyte was soaked into the glass fiber separator. Cyclic voltammetry (CV) and galvanostatic cycling were used for electrochemical characterization. Both methods were performed on the VMP3 potentiostat (Bio-Logic). CV was done in the potential window from 0.01 to 2.5 V vs. Na/Na^+ and scan rates were set to 0.5 mV s^{-1}. Galvanostatic cycling was carried out within a potential window from 0.01 to 2.5 V vs. Na/Na^+. Long-term cycling at 0.2C for 100 cycles was tested for both materials. The second test was cycling at different C-rate from 0.1C up to 5C. The first step was performed as follows: 20 cycles at 0.2C, then 5 cycles at 0.5C, 1C, 2 C and finally at 5C. Subsequently, the C-rate was decreased by the same step to 0.2C with 5 cycles at every C-rate (2C, 1C, 0.5C).

2.4 Instrumentation and characterization methods

2.4.1 MW Synthesis

The Co-Bpdc MOF material was synthesized under ambient atmosphere in a PTFE-lined microwave reactor ERTEC Magnum II (600 W; 2.45 GHz). Microwave power was set to 50 % (300 W) and the reaction was performed in 2 cycles while the duration of each cycle was 20 min with a pause of 5 minutes between them.

2.4.2 Chemical/elemental analyses

The GC-MS measurement of reaction byproducts was performed on an ISQ QD single quadrupole mass spectrometer coupled with a Trace 1300 gas chromatograph by Thermo Scientific. The gas chromatograph was equipped with a Rxi-5ms column (30 m, 0.25 mm, film thickness 0.25 µm) and the temperature program was used as follows: 80 °C to 240 °C with the ramp 10 °C min^{-1}, held at 240 °C for 1 min. Split injection mode (60 ml min^{-1}, split ratio 60) was used with the inlet temperature 280 °C, transfer line and EI source 220 °C (ionization energy: 70 eV, emission current: 30 µA). Cobalt content in Co-Bpdc material was determined by ICP-OES spectroscopy on an iCAP 6500 (Thermo, GB) spectrometer (Co spectral line λ = 238.892 nm).

2.4.3 Structural characterizations

The powder XRD patterns were recorded on a Rigaku MiniFlex 600 diffractometer equipped with a CoK_α (λ = 1.7903 Å) X-ray tube (40 kV, 15 mA). Data processing and crystal size calculations were done with a Rigaku PDXL2 software. The average crystalline size of the crystallites was evaluated using the Scherrer's formula, $d = K\lambda/\beta\cos\theta$, where d is the crystalline size, K is a grain shape dependent constant (0.9), λ is the wavelength, θ is a Bragg reflection angle and β is the full-width half-maximum.

2.4.4 Infrared and Raman spectroscopy

The FTIR spectra were recorded on a Thermo NICOLET 6700 spectrometer using an ATR technique with the diamond crystal (resolution 2 cm^{-1}, 400-4000 cm^{-1}). Raman spectroscopy was performed on a Thermo Raman microscope Nicolet DXR equipped with a He-Ne laser with emission wavelength 633 nm (power 1 and 4 mW). The spectra were recorded from 50 to 2000 cm^{-1}.

2.4.5 X-Ray photoelectron spectroscopy

X-Ray photoelectron spectroscopy measurements were carried out on a SSI X probe spectrometer (model SSI 100, Surface Science Laboratories, Mountain View, CA) equipped with a monochromatized Al-Kα radiation (1486 eV). The sample powders, pressed in small stainless troughs of 4 mm diameter, were placed on an insulating home-made ceramic carousel. The pressure in the analysis chamber was around 10^{-6} Pa. The analyzed area was approximately 1.4 mm^2 and the pass energy was set at 150 eV. The C1s peak of carbon has been fixed to 284.4 eV to set the binding energy scale [52,53]. Data treatment was performed with the CasaXPS program (Casa Software Ltd, UK) and some spectra were deconvoluted with the least squares fitting routine provided by the software with a Gaussian/Lorentzian (85/15) product

function and after subtraction of a nonlinear baseline. To prevent the release of volatiles from the sample, as-prepared sample was heated in N_2 atmosphere at 300 °C prior to analysis.

2.4.6 Thermal analysis and heat treatment

Thermogravimetric analyses were performed on a Setaram LabSys Evo with TG/DSC sensor in an atmosphere of air (heating ramp 10 °C min^{-1}, up to 800 °C, air flow 60 ml min^{-1}) and nitrogen (10 °C min^{-1}, up to 800 °C, 60 ml min^{-1}). Dried powders were heated in a Nabertherm LE 4/11/R6 tube furnace at 800 and 340 °C (5 °C min^{-1}) for 1 hour in an atmosphere of nitrogen and air, respectively.

2.4.7 Microscopy

The scanning electron microscopy and EDX analysis were recorded on a Nova NanoSEM (FEI) with Schottky field emission electron source (0.02–30 keV) and TLD detector at 5 kV. For EDX analysis an EDS platform Octane plus (SDD detector) by EDAX, AMETEK, Inc was used. Transmission electron microscopy (TEM) was carried out on a JEOL JEM 2100 microscope operated at 200 kV (LaB_6 cathode, point resolution 2.3 Å) equipped with OLYMPUS SYS TENGRA camera (2048 x 2048 pixels). Particle size distributions were calculated with the use of OLYMPUS Soft Imaging Solutions software. The powder sample was dispersed in isopropyl alcohol and this suspension was dropped onto a TEM carbon coated copper grid.

2.4.8 Nitrogen adsorption/desorption

Nitrogen adsorption/desorption isotherms were collected at the temperature 77 K on a BELsorp Mini II (Japan). Prior to measurement, the samples were degassed in the BELsorp preparation unit at 100 °C for 19 hours. Surface areas (SA) and total pore volumes (V_{tot} at $p/p_0 = 0.99$) were determined by volumetric techniques [54,55]. The specific surface area was determined by multipoint Brunauer-Emmet-Teller (BET) analysis using at least five data points with relative pressures between 0.05 and 0.30 [54].

2.4.9 Magnetic properties

The magnetization measurements were performed with a Vibrating Sample Magnetometer (Lake Shore 7407, US) at room temperature (300 K) in air atmosphere in a magnetic field range from –760 up to +760 kA m^{-1}.

3 Results and discussion

3.1 Synthesis and materials characterization

The cobalt metal-organic framework material (Co-Bpdc) was synthesized through a microwave-assisted approach based on the solvothermal reaction of Co(II)$(acac)_2$ and biphenyl-4,4′-dicarboxylic acid (Bpdc) in N,N′-dimethylformamide at 160 °C (Figure 1). It is worth noting that no inert atmosphere is required for this reaction. The $Co(acac)_2$ precursor was chosen due to its high solubility in organic solvents and its melting point temperature (ca. 165 °C) which is close to the boiling point of the DMF solvent. It is known that microwaves readily interact with polar hydroxyl groups [56] and thus it can be proposed that the reactivity of biphenyl-4,4′-dicarboxylic acid in the presented system is increased. Such increase of reactivity supports the formation of products and therefore shorter reaction time is expected. As reported, blue-violet coloration is characteristic for tetrahedral coordination of Co(II) ions [57]. Resulting violet colored powder Co-Bpdc material was used as a precursor for the preparation of porous metallic Co nanoparticle/carbon composite discs. The Co-Bpdc material is an advantageous precursor because its stoichiometry is the same throughout the sample, which favors a high homogeneity of final cobalt-carbon composite. For the further application in Na-ion cell, Co-Bpdc MOF material was heated at 340 °C for 1 hour in air to release all volatile byproducts.

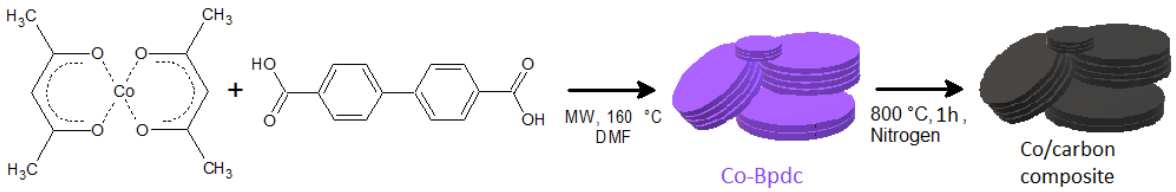


Figure 1: The reaction procedure scheme of materials preparation.

Reaction byproducts were determined by GC-MS analysis of reaction mixture filtrate after microwave-assisted reaction. In the chromatogram acetic acid and acetoin were confirmed (Figure 2S). These species are proposed to be products of decomposition of the acetylacetonate group during the reaction [58].

Powder X-Ray diffraction pattern of as-prepared Co-Bpdc is depicted in Figure 2a. The diffractogram of the Co-Bpdc sample exhibits a number of diffraction lines in the range of 9–40° 2 theta degrees that indicate the crystalline structure characteristic for metal-organic framework materials. After thermal treatment of as-prepared Co-Bpdc sample at 340 °C, an XRD diffractogram (Figure 2a) gave a rise of one intense and relatively broad diffraction peak at 8° and two less intense broad diffractions at 16° and 22° 2 theta degrees, respectively. Since no diffractions peaks of Co_3O_4 oxide appeared we can propose that the structure of metal-organic framework architecture is preserved. However, it can be evidenced that the baseline shape also indicates a presence of some amorphous phase most likely connected with lower crystallinity of Co-Bpdc MOF product. For the sake of comparison, the diffractograms of as-prepared Co-Bpdc, $Co(acac)_2$ precursor and Bpdc linker are given in Supplementary information (Figure 3S). Since there are several reports describing aqueous synthesis of cobalt-based MOF with biphenyl-4,4′-dicarboxylic acid linker [36,42], we made a comparison between diffractogram of our as-prepared Co-Bpdc product and diffractogram of reported structure ($[Co(bpdc)(H_2O)_2].H_2O$, CCDC No. 140986) [36] calculated from single crystal x-ray diffraction data (.CIF file). As illustrated in Supplementary information (Figure 4S), compared diffractograms do not match. Therefore, it can be concluded that our non-aqueous microwave-assisted approach in DMF leads to Co-Bpdc product with specific crystalline structure which is different compared to the published one [36]. Noteworthy, the color of reported crystalline material $[Co(bpdc)(H_2O)_2].H_2O$ with six-coordinated cobalt ions is pink [42], whereas color of our as-prepared Co-Bpdc material is blue-violet, which is assumed to be a result of tetrahedral coordination of cobalt ions [57]. It is proposed that this difference is due to absence of water during presented microwave-assisted synthesis.

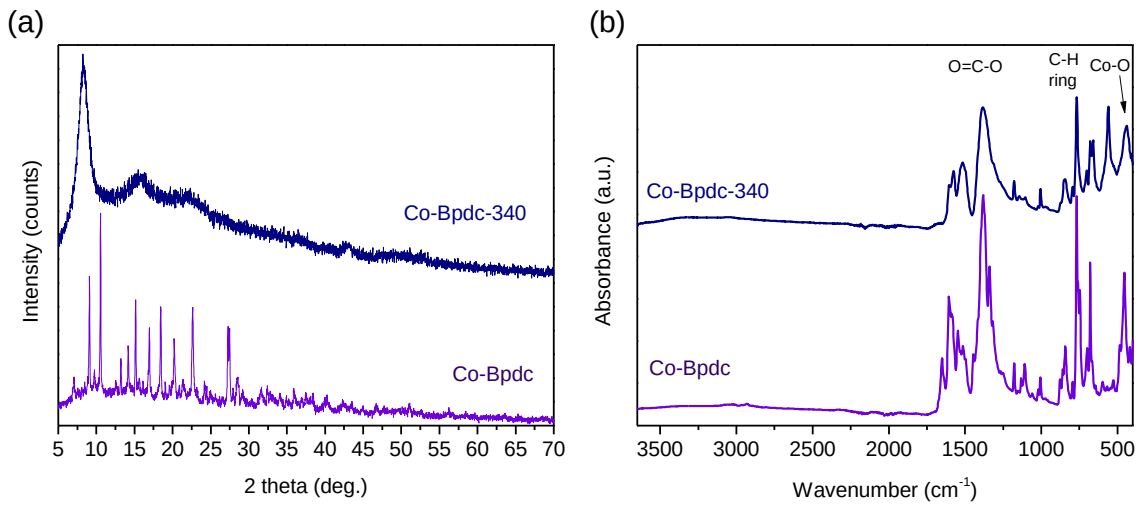


Figure 2. (a) Powder XRD patterns of as-prepared Co-Bpdc and heated Co-Bpdc-340 materials. (b) FTIR spectrum of as-prepared Co-Bpdc and heated Co-Bpdc-340 samples.

Figure 2b displays the FTIR spectrum of as-prepared Co-Bpdc product obtained by microwave-assisted synthesis. Infrared spectra of organic linker and $Co(acac)_2$ precursor are depicted in Supplementary information (Figure 5S). FTIR spectrum of Co-Bpdc sample shows an intense absorption band raised at 1381 cm^{-1} which is attributed to ν_{sym} modes of carboxylate groups whereas the vibrational bands found at 1547, 1589, and 1605 cm^{-1} are characteristic for ν_{asym} vibrations of carboxylate groups. Since the difference between asymmetric and symmetric carboxylate vibrational bands ($\Delta\nu = \nu_{asym} - \nu_{sym}$) is 166 cm^{-1}, bidentate coordination mode of carboxylic acid on cobalt can be assumed [59]. The vibrational bands related to aromatic ring out-of-plane and C–H vibrations are located at 678, 698, and 767 cm^{-1}, respectively [60]. A Co–O bond is assigned to the absorption band at 418 cm^{-1} [61]. The presence of DMF solvent adsorbed on material is connected to the bands at 1109, 1254, 1651, and 2931 cm^{-1} representing deformation vibrations of CH_3, stretch modes of C–C, vibrations of C=O, and stretching of C–H, respectively [62]. It is worth mentioning that the vibrational bands observed in the FTIR spectrum of Co-Bpdc sample are in the good agreement with absorption bands reported in the work describing a metal–organic frameworks containing the biphenyl-4,4′-dicarboxylate linker [31]. FTIR spectrum of thermally treated sample Co-Bpdc-340 exhibits almost similar vibrational bands as as-prepared Co-Bpdc but it must to be stressed out that vibrational bands assigned to DMF solvent [62] do not appear in spectrum of Co-Bpdc-340 sample.

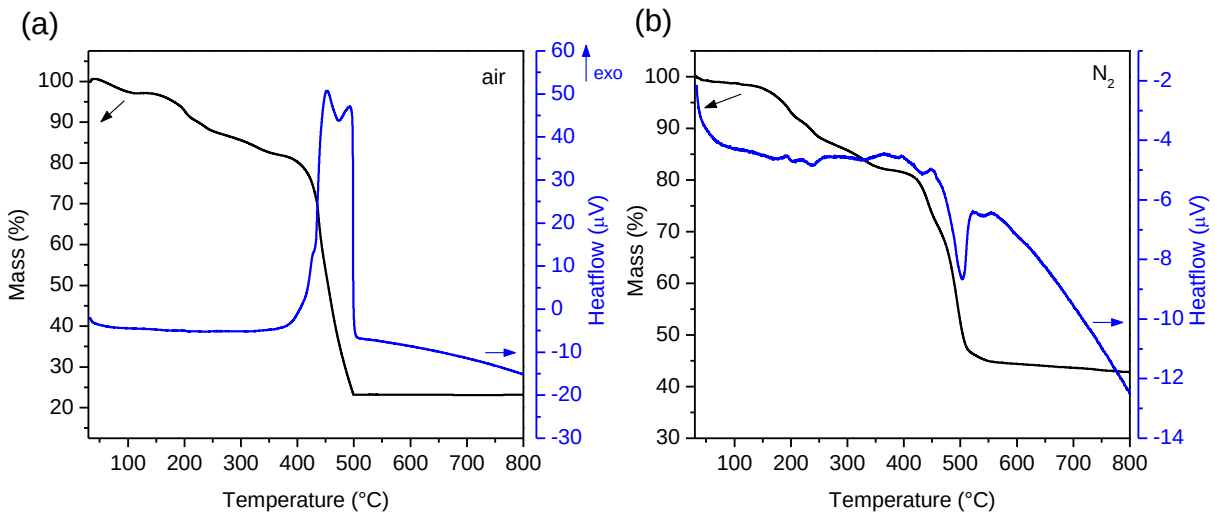


Figure 3. TG/DSC curves of Co-Bpdc sample analysis performed in air (a) and in N_2 atmosphere (b).

Thermal behavior of Co-Bpdc was investigated by TG/DSC method up to 800 °C, in air and in N_2. The TG/DSC curves (Figure 3a) of the measurement performed in air up to 800 °C exhibited three distinguished mass losses in temperature ranges 120–270, 270–370, and 370–500 °C with losses of 10.1, 5.0, and 58.9 %, respectively. The first two losses are attributed to evaporation and release of DMF solvent whereas the highest loss of mass at 370-500 °C represents the oxidation of biphenyl-4,4′-dicarboxylate linker contained in the Co-Bpdc MOF. This step is accompanied by a strong exothermic peak on DSC curve. The residual mass at 800 °C was 23.2 % and according to powder XRD analysis this residue corresponds to Co_3O_4 (JCPDS card no. 073-1701) (Figure 6S). In the case of TG/DSC analysis performed in N_2 up to 800 °C (Figure 3b), the residual mass is 42.8 %. In this case, two mass losses were detected between 110 and 370 °C and between 390 and 570 °C. The first decrease about 16.6 % is due to evaporation of residual DMF and the second mass loss about 37.1 % is assigned to release of CO_2 caused by the decomposition of Co–OC(O) bonds. Time resolved FTIR spectra recorded during this TG analysis are illustrated in Figure 7S. The data from TG analysis can be used to estimate the molecular formula of synthesized Co-Bpdc product. On the basis of the mass losses related to DMF and Bpdc linker, residual content of Co_3O_4 after TG analysis, and the results from TG-FTIR, an approximate formula $Co_{3.0}(Bpdc)_{2.8}(DMF)_{2.3}$ can be proposed for Co-Bpdc. The yield of Co-Bpdc product can be estimated based on its approximate formula (59 %). The product losses originate mainly in the sample manipulation (filtration, washing, etc.).

Figure 4a displays diffraction pattern of Co-C sample obtained after heat treatment of Co-Bpdc in a N_2 atmosphere at 800 °C. Observed diffractions correspond to metallic cobalt nanocrystals (JCPDS card no. 015-0806) and they are characteristic for face-centered cubic (FCC) structure of cobalt and indicate the (111) and (200) facets [63]. An apparent size of cobalt crystallites derived from Scherrer's formula is about 3.7 nm.

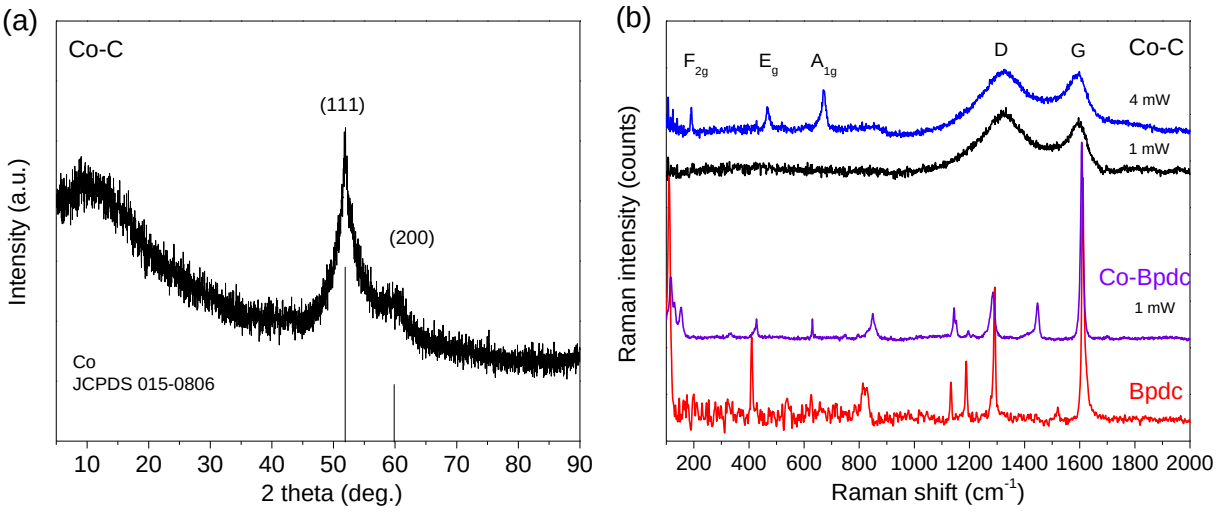


Figure 4. (a) Powder XRD patterns of Co-C product obtained after heat treatment of Co-Bpdc at 800 °C in N_2. Observed diffractions of cobalt nanocrystals match with JCPDS card no. 015-0806. (b) Raman spectra of as-prepared Co-Bpdc material, Bpdc linker (bottom), and Co-C product (upper). The spectra are recorded at the power of 1 and 4 mW.

The Raman spectra of Co-Bpdc and Co-C products are illustrated in Figure 4b. For comparison, Raman spectrum of pure biphenyl-4,4′-dicarboxylic acid (Bpdc linker) is depicted as well (Figure 4b). In the case of the as-prepared Co-Bpdc sample, the bands with the Raman shifts of 1607, 1285, 1144, and 849 cm^{-1} overlap with the bands found in spectrum of Bpdc linker. The band located at 1445 cm^{-1} in Raman spectrum of as-prepared Co-Bpdc is assigned to asymmetric stretch modes of COO^- groups in MOF [64]. The bands observed at 155, 427, and 630 cm^{-1} can be ascribed to vibrations of Co(II)–O species in Co-Bpdc [64]. The Raman spectrum of Co-C sample (Figure 4b) gave a rise of two Raman bands around 1340 and 1587 cm^{-1} (Figure 4b) indicative for the vibration modes of the disordered carbon (D-band) and in-plane vibrations (E_{2g}) of ordered graphitic carbon (G-band), respectively [63,65]. To evaluate the graphitization degree of carbon materials, the intensity ratio of D band and G band (I_D/I_G) was calculated. The I_D/I_G derived from spectrum recorded at 1 mW is 1.15 which indicates the amorphous carbon structure with a high content of defects in plane terminations of disordered

graphitic carbon [65]. The Raman bands at 188, 465, and 668 cm^{-1} appeared in Co-C spectrum after increase of Raman laser power to 4 mW (Figure 4b) are characteristic for F_{2g}, E_g and A_{1g} active Raman modes of Co_3O_4 spinel structure, respectively [66]. The presence of Co_3O_4 in Co-C sample during Raman spectra collection can be explained as a result of laser irradiation which causes local heating effect and photochemically induced oxidation of Co nanoparticles species to Co_3O_4 [67].

The energy-dispersive X-ray spectroscopy was employed to determine the contents of cobalt, carbon, and oxygen in both Co-Bpdc-340 MOF and Co-C nanocomposite samples (Figure 8S, 9S). Both weight and atomic percentage contents together with the residual masses from TG analyses are listed in Table 1. The content of cobalt in Co-Bpdc MOF material was examined by ICP-OES spectroscopy. It was found that as-prepared Co-Bpdc sample contains 16.0 ± 0.1 wt% of cobalt (Table 1). This number is in a good agreement with the cobalt content calculated from residue after TG analysis in air.

Table 1. TG/DSC residual masses and EDX values of C, Co, O element contents.

sample	Co wt% calc.[a]	Co wt% ICP-OES	TG residual mass (%)		sample	EDX wt%			EDX mol%		
			800 °C air	800 °C N_2		C	Co	O	C	Co	O
Co-Bpdc	17.0	16.0 ± 0.1	23.2	42.8	CoC	53.2	44.5	2.3	83.0	14.3	2.7
					Co-Bpdc-340	54.0	25.3	20.7	72.2	7.0	20.8

[a] based on the Co_3O_4 residue after TG analysis in air.

X-Ray photoelectron spectroscopy (XPS) was employed in order to identify the bonding relations between elements in both as-prepared (Co-Bpdc) and carbonized (Co-C) samples (Figure 5) [68]. Survey scans over the whole binding energy range are given in supplementary information (Figure 10S, 11S). As displayed, the peaks for carbon, oxygen, and cobalt are detected. Nitrogen (from DMF) was not found due to its release during heating of as-prepared Co-Bpdc sample at 300 °C prior measurement and also because of the degassing in XPS. This finding is in accordance with TG analysis.

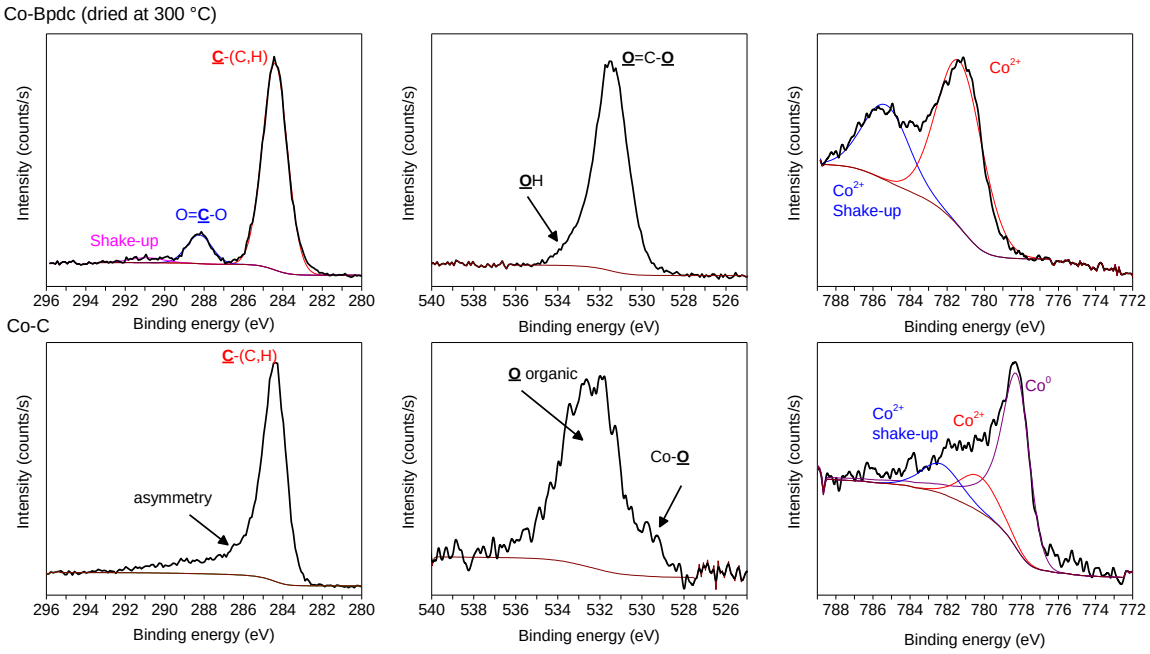


Figure 5. X-Ray photoelectron spectroscopy (XPS) spectra of Co-Bpdc sample (upper) and Co-C nanocomposite (bottom).

Looking closer to the individual elements in the XPS spectra of Co-Bpdc sample (Figure 5, upper), C1s spectrum exhibited three signals with the bonding energies 284.4, 288.2 and 290.9 eV. This latter can be attributed to shake-up satellite peak characteristic of the presence of aromatic ring as expected for Bpdc [69]. In this case, the two first components may be assigned respectively to **C**-(C,H) of the aromatic rings and to O=**C**-O carboxylate groups. However, the **C**-(C,H)/O=**C**-O ratio (7.4) is slightly higher than the one expected for pure Bpdc (6) but this difference can easily be explained by the presence of a small amount of carbon contamination, as frequently encountered with XPS measurement [52,68]. The major part of the O 1s peak is measured at 531.4 eV and can be attributed to carboxylate oxygen atoms with bidentate coordination to Co. The O1s shoulder part, in the high BE side, can be understood as the remaining of unreacted acidic form of the Bpdc and/or from other –OH groups that could appear with surface moisture. The Co $2p_{3/2}$ spectrum of Co-Bpdc sample showed two signals characteristic of the presence of Co^{2+} with the main peak detected at 781.3 and its satellite structures around 785 eV [70].

Co-C composite sample obtained after heat treatment in N_2 displayed in C1s spectrum the most intense peak with binding energy 284.4 eV (Figure 5). Particularly, the asymmetry of the main component in the high BE side could be associated with the simultaneous presence of oxidized carbon species and graphitic-like compounds, this latter presenting intrinsic asymmetry of the

C1s peak. The presence of oxidized carbon species can be confirmed by the detection of a broad component in the high BE side of the O1s peak, corresponding to organic oxygen species that could be attributed to the residue coming from incomplete carbonization of Bpdc. O1s peak at 529.5 eV is assigned to the oxygen in Co**O** indicating small amount of oxidized Co nanoparticles caused most probably by exposing the sample to air. The Co $2p_{3/2}$ spectrum reveals the major presence of reduced Co^0 associated with oxidized Co^{2+} species. As displayed, the most intense band detected at 778.3 eV is related to Co^0, which confirms major presence of cobalt nanoparticles while the two other bands, 780.3 and 782.4 eV can be respectively attributed to the main peak and its satellite for Co^{2+}. This observation is in accordance with the published data for metallic cobalt particles and Co^{2+} valence in CoO oxide [18,70]. Noteworthily, for the application of Co-C materials in sodium-ion batteries, the content of oxidized cobalt species is not considered as a defective feature [1].

Figure 6a-d illustrates SEM images of MOF sample Co-Bpdc-340 and the sample after heat treatment in N_2 atmosphere (Co-C). The SEM image of as-prepared Co-Bpdc MOF material is provided in Supplementary information as Figure 12S.

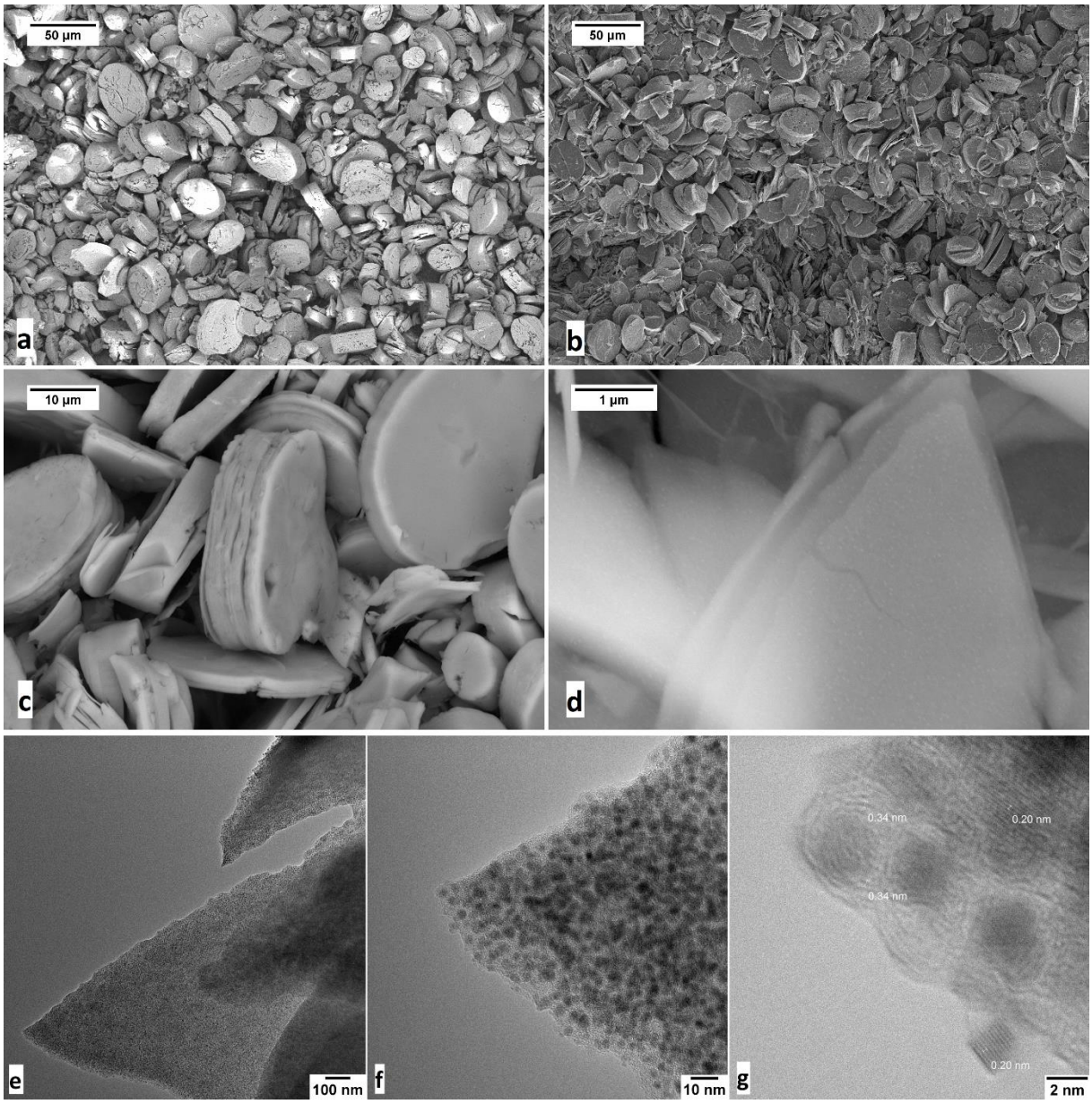


Figure 6. SEM images of Co-Bpdc-340 material (a) and Co-C nanocomposite (b-d). TEM images of Co-C nanocomposite (e-g).

The as-prepared Co-Bpdc MOF (Figure 12S) and Co-Bpdc-340 (Figure 6a) sample exhibited a platelet-like morphology formed by the superposition of disc particles. Compared to 2D nanoplates structure of cobalt MOF prepared from biphenyl-4,4′-dicarboxylic acid via aqueous approach by Zhang et al. [42], our Co-Bpdc material exhibit well defined structure of layered discs. This architecture of layered disc plates appears to be preserved in the Co-C nanocomposites obtained after thermal treatment in N_2 (Figure 6b, c, d). Such morphology might be a consequence of molecular geometry of Co-Bpdc product due to probably tetrahedral coordination environment of Co^{2+} ions (see discussion on XRD analyses). According to SEM

images, it can be argued that the layered plate-like disc morphology is well defined and the distribution and coverage of cobalt nanoparticles is homogeneous, since no separation of big nanoparticle agglomerates was detected. Transmission electron microscopy was employed in order to study products morphology in deeper insight. The Co-Bpdc-340 MOF product exhibited structure without the presence of nanoparticles (Figure 13S). The TEM images of Co-C sample (Figure 6e-g) revealed cobalt nanoparticles dispersed in the carbon matrix. The average size of the nanoparticles is about 4 nm and it is in the accordance with the results from powder XRD analysis determined by Scherrer equation (3.7 nm) (Figure 4a). Since cobalt nanoparticles are tightly embedded in the carbon matrix, their aggregation is hampered, resulting in their small size and homogeneous dispersion in final material. The Co nanocrystal lattice fringes observed in the TEM image depicted in Supporting materials exhibit a plane distance 0.20 nm which is indicative for the (111) facets of metallic face-centered cubic (FCC) Co structure [47,63]. Furthermore, the carbon surrounding the Co nanoparticles (Figure 6g, 14S) presented the d-spacing of ca. 0.35 nm, which coincides with the (002) crystal plane of graphitic carbon, indicating a partial degree of transformation from amorphous carbon to disordered graphitic carbon as reported in the other works [63,71].

Co-Bpdc and Co-C samples were characterized by N_2-physisorption. The adsorption/desorption isotherms are displayed in Figure 7a. Surface area of Co-Bpdc and Co-C samples was determined by BET method [54]. As-prepared sample (Co-Bpdc) exhibited almost nonporous character, with a low specific surface area (4 $m^2\ g^{-1}$) and very low pore volume (0.02 $cm^3\ g^{-1}$). Surface area of the sample Co-Bpdc-340 was 4 $m^2\ g^{-1}$ which is the same as in case of as-prepared Co-Bpdc sample. N_2-adsorption/desorption isotherms of Co-Bpdc-340 sample are given in supplementary information (Figure 15S). However, after heat treatment of Co-Bpdc product in nitrogen at 800 °C, surface area and pore volume increased significantly to 366 $m^2\ g^{-1}$ and 0.16 $cm^3\ g^{-1}$, respectively. As illustrated in Figure 7a, the nitrogen adsorption takes place at a low relative pressure indicating the presence of micropores ($d_p < 2$ nm).

Figure 7b shows magnetization hysteresis curves of the Co-C in the magnetic field range from –760 up to 760 kA m^{-1} at 300 K. Clearly, the Co-C sample exhibits the ferromagnetic hysteresis loops, due to the contribution of metallic Co NPs [47]. The saturation magnetization value of the Co-C is measured to be 51 A $m^2\ kg^{-1}$, which is lower than that reported for bulk Co (168 A $m^2\ kg^{-1}$) [72], which is caused mainly by the negative contribution of the nonmagnetic carbon matrix. Important feature which have to also be considered is particle size. It can be argued, that smaller particles introduce more surface disorders than bulk material. These surface

disorders exhibit a nonmagnetic behavior resulting in magnetization saturation decrease. However, the value of 51 A m^2 kg^{-1} is still higher than that of previously reported Co/C materials [73,74]. Such magnetic behavior can be interesting for further applications, for example in field of catalysis or adsorption techniques [73].

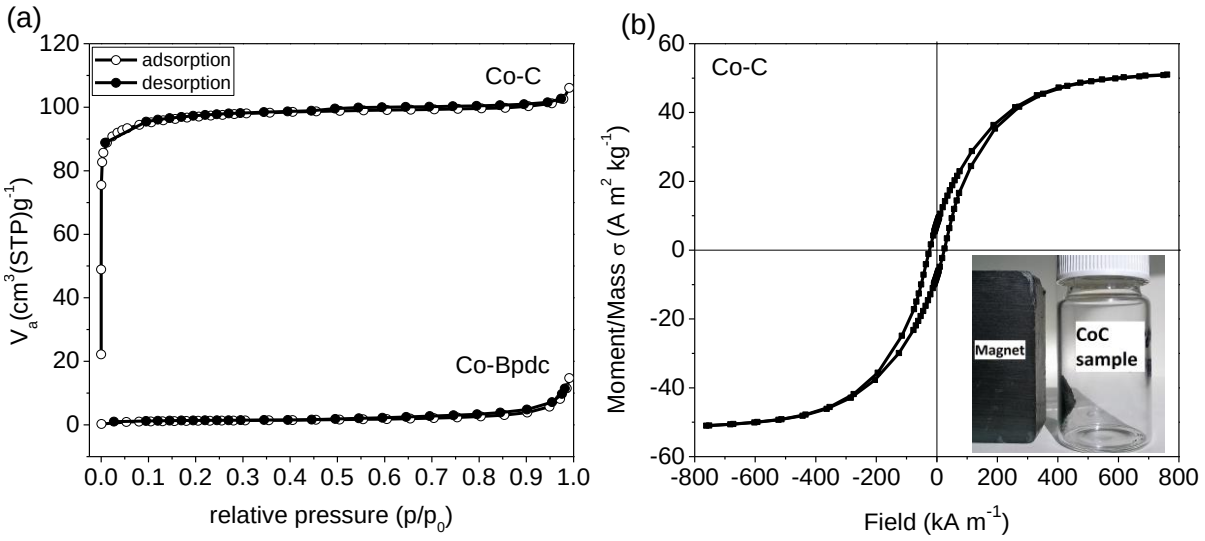


Figure 7. (a) Nitrogen adsorption/desorption isotherms of as-prepared Co-Bpdc material (bottom) and Co-C nanocomposite product (upper). (b) Magnetization curves of Co-C nanocomposite sample.

3.2 Electrochemical characterization

Co-Bpdc-340 sample and Co-C nanocomposite disc material were used to prepare electrodes for the characterization of their electrochemical properties. Since there are several reports describing an utilization of Co-based MOF materials Na-ion batteries [40,42], we investigated our Co-Bpdc-340 sample prepared via non-aqueous MW-assisted approach as an electrode material in Na-ion battery. As reported in the work of Zhang and coworkers, the MOF constructed from biphenyl-4,4′-dicarboxylic acid linker exhibits the cell volume optimal to facilitate the insertion/extraction of Na^+ [42]. Moreover, the layered architecture of Co-Bpdc-340 is proposed to support insertion/extraction of Na^+. The electrochemical properties of the Co-Bpdc-340 sample and Co-C nanocomposite material were tested in Na-ion system.

The first step was a cyclic voltammetry (CV) with the scan rate of 0.5 mV s^{-1} (Figure 8). The CV curves of Co-Bpdc-340 sample are shown in Figure 8a. Electrochemical activity of the electrode is increasing with the cycle. As displayed, Co-Bpdc-340 exhibit one anodic peak and two cathodic peaks. A sharp anodic peak was observed at 0.68 V vs. Na/Na^+. Two cathodic

peaks were found at 0.24 V and 0.01 V vs. Na/Na^+. One cathodic peak was found at 0.24 V. An activity close to 0.01 V vs. Na/Na^+ is probably caused by a shift from the equilibrium potential.

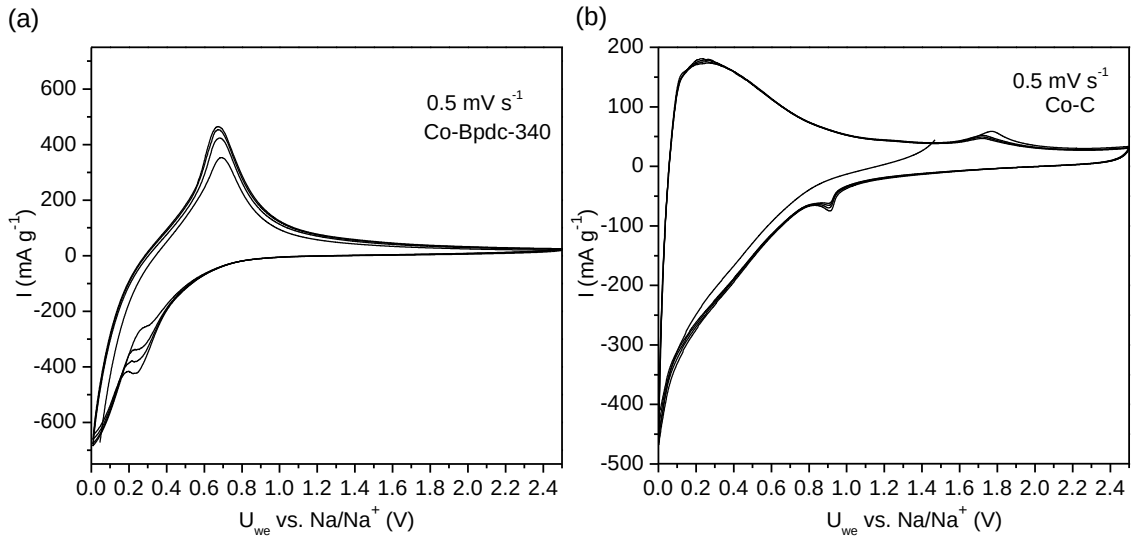


Figure 8. Cyclic voltammetry of (a) Co-Bpdc-340 MOF and (b) Co-C nanocomposite vs.sodium at 0.5 mV s^{-1}.

CV of Co-C sample is shown in Figure 8b and according to the recorded curves stable electrochemical activity of Co-C sample can be testified. There are two main redox peaks distinguished on CV curves. The first anodic peak is found at 0.21 V and the second at 1.77 V. The cathodic peaks are located at 0.91 and 0.05 V vs. Na/Na^+, respectively. Both materials are electrochemically active in the range close to 0 V vs Na/Na^+ which makes them suitable candidates for the anodes of Na-ion accumulators. We can also see a big difference between the shape of curves of these materials caused by the redox behavior of Co-Bpdc and Co-C samples. Based on the results from CV, electrochemical surface areas (ECSA) were calculated for both samples [75]. The ECSA of Co-C composite and Co-Bpdc-340 sample was 96 and 42 $m^2\ g^{-1}$, respectively.

As a next step, two charge/discharge cycles at 25 mA g^{-1} for capacity determination were performed (Figure 9). Significant difference between charge/discharge curve profiles of the Co-Bpdc-340 and Co-C nanocomposite sample was evidenced. The charge and discharge profiles of these materials correspond with data obtained by cycling voltammetry (Figure 8). The Co-Bpdc-340 sample (Figure 9a) exhibited stable charge plateau at 0.4 V vs. Na/Na^+ and discharge plateau at 0.5 V vs. Na/Na^+ which is in correlation with sharp cathodic and anodic peaks

observed during CV measurement (Figure 8). On the other hand, the Co-C nanocomposite (Figure 9b) exhibited very slow potential drop between 1.5 V and 0.01 V vs. Na/Na^+ within charging and very slow potential increase during discharging without any stable plateau. As illustrated in Figure 9, the capacity of both samples in the second discharge cycle was almost similar. In case of Co-Bpdc-340 and Co-C sample the capacity reached 222 mA h g^{-1} and 210 mA h g^{-1}, respectively. Co-Bpdc-340 sample exhibit capacity retention about 81.3% in the first cycle and 95.7 % in the second cycle (Figure 9a). The capacity retention of Co-C nanocomposite sample reached 68.6 % and 81.1 % in the first and in the second cycle, respectively (Figure 9b). Generally, the capacity retention in the first cycle for both samples is quite high, especially in the case of the sample Co-Bpdc-340 (81.3 %). Zhang et al. [42] and Dong et al. [40] described cobalt based MOF anodes with capacity retention in the first cycle around 25 % which is much lower compared to our results. In addition, the capacity retention achieved with Co-Bpdc-340 sample in the first cycle was also higher than capacity retention of hard (69 and 72 %) or sphere (62 %) carbon materials reported by Pol et al. [76], Sun et al. [77], and Li et al. [78].

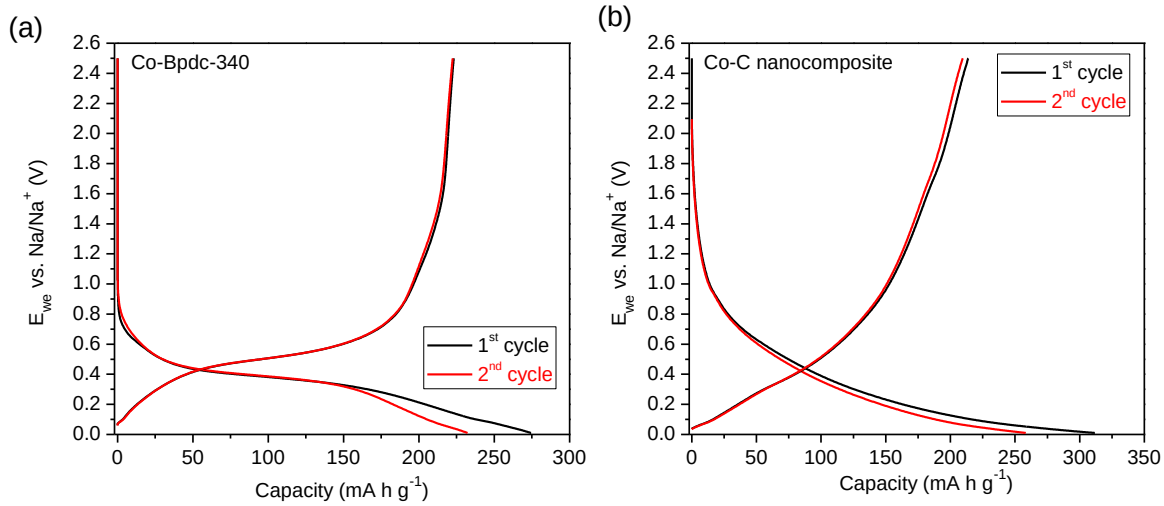


Figure 9. Two charge/discharge cycles of (a) Co-Bpdc-340 sample and (b) Co-C nanocomposite recorded at 25 mA g^{-1}.

To further investigate the electrochemical performance of Na-ion cells with Co-Bpdc and Co-C anode materials, galvanostatic cycling was employed. As an 1C current, the value of 200 mA g^{-1} was chosen. Cycling of Na-ion cell with Co-Bpdc-340 sample is displayed in Figure 10. The Co-Bpdc-340 sample was cycled at different C-rates up to 5C (Figure 10a). As

displayed, the Co-Bpdc-340 sample delivered a high initial capacity 196 mA h g^{-1} in the first cycle at 0.2C. After first twenty cycles at 0.2C its capacity dropped about 6 %. The capacity in the last cycle during increasing C-rate at 0.5C, 1C, 2C and 5 C was 145 mA h g^{-1}, 113 mA h g^{-1}, 77 mA h g^{-1} and 15 mA h g^{-1}, respectively. According to data illustrated in Figure 10a, we can conclude that Co-Bpdc-340 sample is very sensitive to increasing load. Within C-rate reducing, the Co-Bpdc-340 sample shown very stable behavior and reached similar capacities as in the previous cycles (Figure 10a). An overall capacity retention achieved for Co-Bpdc-340 after 60 cycles at different C-rate was 91.9 %. For example, the capacity retention after 40 cycles at different C-rate reported by Zhang et al. was 79.2 % [42]. Dong et al. evidenced capacity retention 28.2 % after 60 cycles at different C-rate [40]. Indeed, these reported values are lower than capacity retention observed for the sample Co-Bpdc-340.

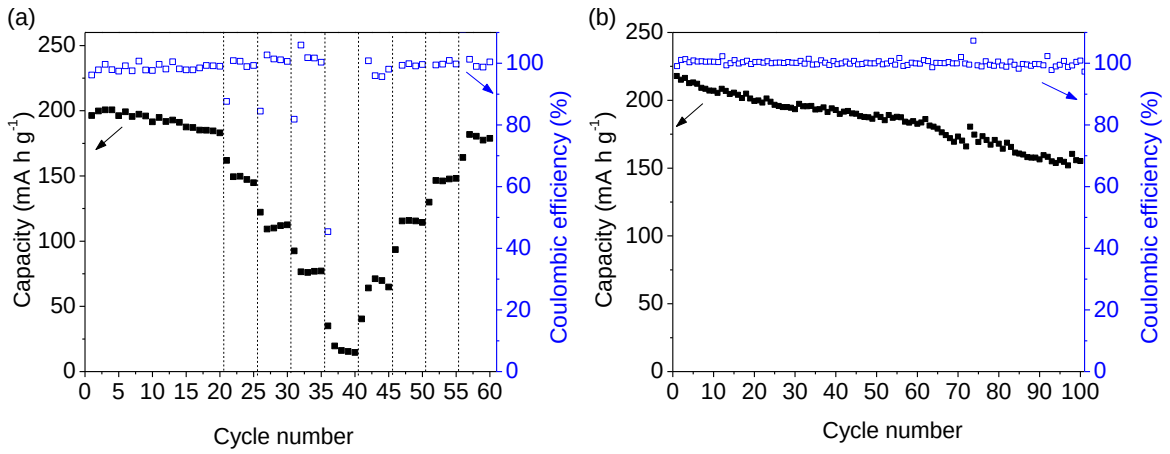


Figure 10. (a) The capacities achieved during cycling of Co-Bpdc-340 MOF sample vs. sodium at different C-rates. (b) The capacity during cycling at 0.2 C Co-Bpdc-340 sample vs. sodium.

A long-term cycling performance of the Co-Bpdc-340 sample at 0.2C is depicted in Figure 10b. The Co-Bpdc-340 sample exhibited initial capacity 218 mA h g^{-1}. The capacity after 100 cycles was 156 mA h g^{-1} which corresponds to capacity retention 71.6 % (capacity loss 0.28 % per cycle). For example, in recent work of Zhang et al., the capacity retention after 50 cycles at 20 mA g^{-1} was 82 % and this number is equal to 0.36 % capacity drop per cycle [42]. Dong et al. reported Co-MOF based anode with high initial capacity around 850 mAh g^{-1}. However, due to low capacity retention (ca. 25 %), the capacity in the second cycle was almost a half. After 150 cycles at 100 mA g^{-1}, reported Co-MOF based anode delivered capacity 152 mAh g^{-1} which corresponds to 18% capacity retention (capacity drop 0.55 % per cycle) [40]. Compared

to the results presented by Zhang et al. [42] and Dong et al. [40], we can conclude that the capacity loss per cycle evidenced in our case is significantly lower indicating better stability of Co-Bpdc-340 anode material.

The same testing procedure as in case of Co-Bpdc-340 sample was also applied for characterization of the Co-C nanocomposite in Na-ion system. Galvanostatic cycling at different C-rates is displayed in Figure 11. The initial capacity of Co-C nanocomposite achieved in the first cycle (0.2C) was 172 mAh g^{-1}. After 20 cycles at 0.2C, the capacity dropped to 117 mAh g^{-1}. Subsequently, the load was increased to 5C and then decreased back to 0.2C. As seen from Figure 11a, the Co-C material is even more sensitive than Co-Bpdc-340 sample to used load and capacity decreased rapidly with increasing C-rate. The capacity after 60 cycles at different C-rates was 100 mAh g^{-1} which corresponds to capacity retention 58 %. Next step involved 60 cycles at 0.2C rate, see Figure 11b. The capacity at the beginning of cycling was 190 mAh g^{-1} and the capacity retention during the first cycle was 74 %. This capacity at the C-rate of 0.2C (40 mA g^{-1}) is higher than the capacities reported by Pol et al. [76] (125 mAh g^{-1} at 30 mA g^{-1}), Wenzel et al. [79] (130 mAh g^{-1} at 0.2C) or Chen et al. [80] (Sample SC700 155 mAh g^{-1} at 30 mA g^{-1}). The capacity after Co-C nanocomposite cycling was 96 mAh g^{-1} which corresponds to capacity retention of 51 %.

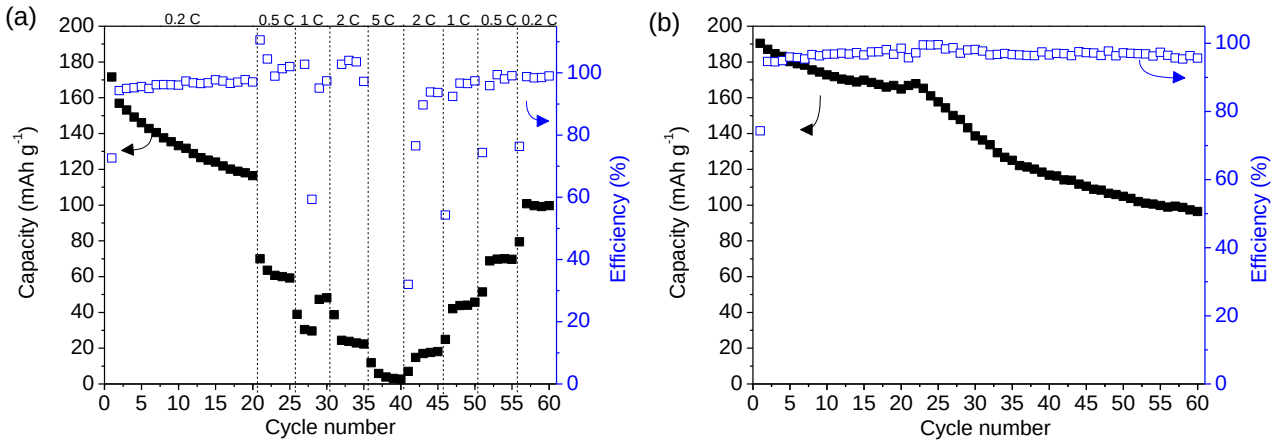


Figure 11. (a) The capacities achieved during cycling of Co-C nanocomposite vs. sodium at different C-rates. (b) The capacity during cycling at 0.2C Co-C vs. sodium.

Based on the performed measurements it can be concluded that Co-Bpdc-340 and Co-C samples derived from Co-Bpdc MOF material exhibit different electrochemical behavior. This

difference is proposed to be caused by specific material structure affected by thermal treatment of as-prepared Co-Bpdc MOF. Due to the MOF structure, which seems to be preserved in case of Co-Bpdc-340 sample, higher polarity is assumed and therefore the electrochemical performance is enhanced in comparison with Co-C sample. Definitely, it was demonstrated that both materials prepared from Co-Bpdc MOF can be successfully utilized in Na-ion cell.

4 Conclusion

In this work we presented facile microwave-assisted synthesis of platelet-like cobalt-biphenyl-4,4'-dicarboxylate metal-organic framework (Co-Bpdc) from cobalt(II) acetylacetonate and biphenyl-4,4'-dicarboxylic acid in N,N'-dimethylformamide solvent. Violet product labeled as Co-Bpdc exhibits unique morphology of platelet-like discs. As we demonstrated, this product was used as a precursor for preparation of porous cobalt-carbon nanocomposite. Nanocomposite product (Co-C) was obtained via thermal treatment in nitrogen atmosphere at 800 °C. Surface area of Co-C product reached 366 m^2 g^{-1} and microporous character was evidenced. Co-C nanocomposite revealed well defined morphology of layered platelet-like discs with a homogeneous distribution of metallic cobalt nanoparticles (4 nm) embedded in the carbon matrix. From this point of view, the Co-Bpdc material obtained via microwave-assisted synthesis is proposed as a suitable precursor for the preparation of homogenous nanocomposite of cobalt nanoparticles and carbon. Indeed, we proved, that both Co-Bpdc MOF and Co-C nanocomposite disc material are electrochemically active Na-ion systems. The initial capacities achieved for Co-Bpdc-340 and Co-C nanocomposite were over 220 and 200 mAh g^{-1}, respectively. Primarily, the material Co-Bpdc-340 exhibits high capacity retention and good stability after cycling at different C-rate. The Co-Bpdc-340 and Co-C material are promising anode materials for practical Na-ion batteries thanks to their easy preparation and fast synthesis. Interestingly, a ferromagnetic behavior was observed, indicating some other possible applications (catalysis, adsorption, separation).

Acknowledgement

This work was supported by the Ministry of Education, Youth and Sports of the Czech Republic - Program NPU I (LO1504) and (LTT19001). This contribution was written with support of Operational Program Research and Development for Innovations co-funded by the European Regional Development Fund (ERDF) and national budget of Czech Republic, within the

framework of project CPS - strengthening research capacity (reg. number: CZ.1.05/2.1.00/19.0409). The support by BUT specific research programme (project No. FEKT-S-17-4595) is gratefully acknowledged.

References

[1] N. Yabuuchi, K. Kubota, M. Dahbi, S. Komaba, Research development on sodium-ion batteries, Chem. Rev. 114 (2014) 11636–11682. doi:10.1021/cr500192f.

[2] S.Y. Hong, Y. Kim, Y. Park, A. Choi, N.-S. Choi, K.T. Lee, Charge carriers in rechargeable batteries: Na ions vs. Li ions, Energy Environ. Sci. 6 (2013) 2067. doi:10.1039/c3ee40811f.

[3] Y. Liang, W.-H. Lai, Z. Miao, S.-L. Chou, Nanocomposite Materials for the Sodium-Ion Battery: A Review, Small. 14 (2018) 1702514. doi:10.1002/smll.201702514.

[4] M.Z. Krolow, C.A. Hartwig, G.C. Link, C.W. Raubach, J.S.F. Pereira, R.S. Picoloto, M.R.F. Gonçalves, NanoCarbon 2011, Springer Berlin Heidelberg, Berlin, Heidelberg, 2013. doi:10.1007/978-3-642-31960-0.

[5] T. Gupta, Carbon Composites and Related Metal Matrix, in: Carbon N. Y., Springer International Publishing, Cham, 2018: pp. 71–87. doi:10.1007/978-3-319-66405-7_3.

[6] N. Nitta, F. Wu, J.T. Lee, G. Yushin, Li-ion battery materials: present and future, Mater. Today. 18 (2015) 252–264. doi:10.1016/j.mattod.2014.10.040.

[7] H.D. Yoo, E. Markevich, G. Salitra, D. Sharon, D. Aurbach, On the challenge of developing advanced technologies for electrochemical energy storage and conversion, Mater. Today. 17 (2014) 110–121. doi:10.1016/j.mattod.2014.02.014.

[8] M.-S. Balogun, Y. Luo, W. Qiu, P. Liu, Y. Tong, A review of carbon materials and their composites with alloy metals for sodium ion battery anodes, Carbon N. Y. 98 (2016) 162–178. doi:10.1016/j.carbon.2015.09.091.

[9] D. Kundu, E. Talaie, V. Duffort, L.F. Nazar, The emerging chemistry of sodium ion batteries for electrochemical energy storage, Angew. Chemie - Int. Ed. 54 (2015) 3432–3448. doi:10.1002/anie.201410376.

[10] D.A. Stevens, J.R. Dahn, The Mechanisms of Lithium and Sodium Insertion in Carbon Materials, J. Electrochem. Soc. 148 (2001) A803. doi:10.1149/1.1379565.

[11] X. Zhou, Y.-G. Guo, Highly Disordered Carbon as a Superior Anode Material for Room-Temperature Sodium-Ion Batteries, ChemElectroChem. 1 (2014) 83–86. doi:10.1002/celc.201300071.

[12] T. Chen, Y. Liu, L. Pan, T. Lu, Y. Yao, Z. Sun, D.H.C. Chua, Q. Chen, Electrospun carbon nanofibers as anode materials for sodium ion batteries with excellent cycle performance, J. Mater. Chem. A. 2 (2014) 4117. doi:10.1039/c3ta14806h.

[13] S. Komaba, W. Murata, T. Ishikawa, N. Yabuuchi, T. Ozeki, T. Nakayama, A. Ogata, K. Gotoh, K. Fujiwara, Electrochemical Na Insertion and Solid Electrolyte Interphase for Hard-Carbon Electrodes and Application to Na-Ion Batteries, Adv. Funct. Mater. 21 (2011) 3859–3867. doi:10.1002/adfm.201100854.

[14] X. Dou, I. Hasa, D. Saurel, C. Vaalma, L. Wu, D. Buchholz, D. Bresser, S. Komaba, S. Passerini, Hard carbons for sodium-ion batteries: Structure, analysis, sustainability, and electrochemistry, Mater. Today. 23 (2019) 87–104. doi:10.1016/j.mattod.2018.12.040.

[15] C. Wu, Y. Jiang, P. Kopold, P.A. van Aken, J. Maier, Y. Yu, Peapod-Like Carbon-Encapsulated Cobalt Chalcogenide Nanowires as Cycle-Stable and High-Rate Materials for Sodium-Ion Anodes, Adv. Mater. 28 (2016) 7276–7283. doi:10.1002/adma.201600964.

[16] C. An, Y. Wang, Y. Xu, Y. Wang, Y. Huang, L. Jiao, H. Yuan, In Situ Preparation of 1D Co@C Composite Nanorods as Negative Materials for Alkaline Secondary Batteries, ACS Appl. Mater. Interfaces. 6 (2014) 3863–3869. doi:10.1021/am4048392.

[17] X. Xu, J. Shen, N. Li, M. Ye, Microwave-assisted in situ synthesis of cobalt nanoparticles decorated on reduced graphene oxide as promising electrodes for supercapacitors, Int. J. Hydrogen Energy. 40 (2015) 13003–13013. doi:10.1016/j.ijhydene.2015.08.021.

[18] X. Sun, G.-P. Hao, X. Lu, L. Xi, B. Liu, W. Si, C. Ma, Q. Liu, Q. Zhang, S. Kaskel, O.G. Schmidt, High-defect hydrophilic carbon cuboids anchored with Co/CoO nanoparticles as highly efficient and ultra-stable lithium-ion battery anodes, J. Mater. Chem. A. 4 (2016) 10166–10173. doi:10.1039/C6TA03098J.

[19] V. Etacheri, C. Hong, J. Tang, V.G. Pol, Cobalt nanoparticles chemically bonded to porous carbon nanosheets: A stable high-capacity anode for fast-charging lithium-ion batteries, ACS Appl. Mater. Interfaces. (2018) acsami.7b15915. doi:10.1021/acsami.7b15915.

[20] L. Hu, Q. Chen, Hollow/porous nanostructures derived from nanoscale metal–organic frameworks towards high performance anodes for lithium-ion batteries, Nanoscale. 6 (2014) 1236–1257. doi:10.1039/C3NR05192G.

[21] F. Zheng, G. Xia, Y. Yang, Q. Chen, MOF-derived ultrafine MnO nanocrystals embedded in a porous carbon matrix as high-performance anodes for lithium-ion batteries, Nanoscale. 7 (2015) 9637–9645. doi:10.1039/C5NR00528K.

[22] B. Chen, G. Ma, Y. Zhu, Y. Xia, Metal-organic-frameworks derived cobalt embedded in various carbon structures as bifunctional electrocatalysts for oxygen reduction and evolution reactions, Sci. Rep. 7 (2017) 5266. doi:10.1038/s41598-017-05636-y.

[23] H. Furukawa, K.E. Cordova, M. O'Keeffe, O.M. Yaghi, The Chemistry and Applications of Metal-Organic Frameworks, Science (80-.). 341 (2013) 1230444–1230444. doi:10.1126/science.1230444.

[24] J. Liu, C. Wöll, Surface-supported metal–organic framework thin films: fabrication methods, applications, and challenges, Chem. Soc. Rev. 46 (2017) 5730–5770. doi:10.1039/C7CS00315C.

[25] J.L.C. Rowsell, O.M. Yaghi, Metal–organic frameworks: a new class of porous materials, Microporous Mesoporous Mater. 73 (2004) 3–14. doi:10.1016/j.micromeso.2004.03.034.

[26] S. Yuan, L. Zou, J.-S. Qin, J. Li, L. Huang, L. Feng, X. Wang, M. Bosch, A. Alsalme, T. Cagin, H.-C. Zhou, Construction of hierarchically porous metal–organic frameworks through linker labilization, Nat. Commun. 8 (2017) 15356. doi:10.1038/ncomms15356.

[27] E. Flage-Larsen, K. Thorshaug, Linker conformation effects on the band gap in metal-organic frameworks, Inorg. Chem. 53 (2014) 2569–2572. doi:10.1021/ic4028628.

[28] C.K. Lin, D. Zhao, W.Y. Gao, Z. Yang, J. Ye, T. Xu, Q. Ge, S. Ma, D.J. Liu, Tunability of band gaps in metal-organic frameworks, Inorg. Chem. 51 (2012) 9039–9044. doi:10.1021/ic301189m.

[29] P. Deria, J.E. Mondloch, O. Karagiaridi, W. Bury, J.T. Hupp, O.K. Farha, Beyond post-synthesis modification: evolution of metal–organic frameworks via building block replacement, Chem. Soc. Rev. 43 (2014) 5896–5912. doi:10.1039/C4CS00067F.

[30] W. Lu, Z. Wei, Z.-Y. Gu, T.-F. Liu, J. Park, J. Park, J. Tian, M. Zhang, Q. Zhang, T. Gentle III, M. Bosch, H.-C. Zhou, Tuning the structure and function of metal–organic frameworks via linker design, Chem. Soc. Rev. 43 (2014) 5561–5593. doi:10.1039/C4CS00003J.

[31] R.-Q. Zhong, R.-Q. Zou, M. Du, T. Yamada, G. Maruta, S. Takeda, J. Li, Q. Xu, Metal–organic frameworks of manganese(II) 4,4′-biphenyldicarboxylates: crystal structures, hydrogen adsorption, and magnetism properties, CrystEngComm. 12 (2010) 677–681. doi:10.1039/B916168F.

[32] N.A. Khan, S.H. Jhung, Synthesis of metal-organic frameworks (MOFs) with microwave or ultrasound: Rapid reaction, phase-selectivity, and size reduction, Coord. Chem. Rev. 285 (2015) 11–23. doi:10.1016/j.ccr.2014.10.008.

[33] X. Wu, Z. Bao, B. Yuan, J. Wang, Y. Sun, H. Luo, S. Deng, Microwave synthesis and characterization of MOF-74 (M = Ni, Mg) for gas separation, Microporous Mesoporous Mater. 180 (2013) 114–122. doi:10.1016/j.micromeso.2013.06.023.

[34] H.Y. Cho, D.A. Yang, J. Kim, S.Y. Jeong, W.S. Ahn, CO 2 adsorption and catalytic application of Co-MOF-74 synthesized by microwave heating, Catal. Today. 185 (2012) 35–40. doi:10.1016/j.cattod.2011.08.019.

[35] J.-M. Rueff, S. Pillet, G. Bonaventure, M. Souhassou, P. Rabu, Synthesis, Structure and Magnetic Properties of the Cobalt(II) 1,1′-Biphenyl-2,2′-dicarboxylate Hydroxide Chain Compound [Co3{O2CC12H8CO2}2.5(OH)(H2O)2]n, Eur. J. Inorg. Chem. 2003 (2003) 4173–4178. doi:10.1002/ejic.200300267.

[36] L. Pan, N. Ching, X. Huang, J. Li, Reactions and Reactivity of Co−bpdc Coordination Polymers (bpdc = 4,4‘-biphenyldicarboxylate), Inorg. Chem. 39 (2000) 5333–5340. doi:10.1021/ic0004939.

[37] K.K. Gangu, S. Maddila, S.B. Jonnalagadda, A review on synthesis, crystal structure and functionality of naphthalenedicarboxylate ligated metal-organic frameworks, Inorganica Chim. Acta. 466 (2017) 308–323. doi:10.1016/j.ica.2017.06.038.

[38] L. Wang, Y. Han, X. Feng, J. Zhou, P. Qi, B. Wang, Metal–organic frameworks for energy storage: Batteries and supercapacitors, Coord. Chem. Rev. 307 (2016) 361–381. doi:10.1016/j.ccr.2015.09.002.

[39] P. Nie, L. Shen, G. Pang, Y. Zhu, G. Xu, Y. Qing, H. Dou, X. Zhang, Flexible metal–organic frameworks as superior cathodes for rechargeable sodium-ion batteries, J. Mater. Chem. A. 3 (2015) 16590–16597. doi:10.1039/C5TA03197D.

[40] C. Dong, L. Xu, Cobalt- and Cadmium-Based Metal–Organic Frameworks as High-Performance Anodes for Sodium Ion Batteries and Lithium Ion Batteries, ACS Appl. Mater. Interfaces. 9 (2017) 7160–7168. doi:10.1021/acsami.6b15757.

[41] Z. Wang, H. Tao, Y. Yue, Metal-Organic-Framework-Based Cathodes for Enhancing the Electrochemical Performances of Batteries: A Review, ChemElectroChem. (2019) celc.201900843. doi:10.1002/celc.201900843.

[42] Y. Zhang, S. Yang, X. Chang, H. Guo, Y. Li, M. Wang, W. Li, L. Jiao, Y. Wang, MOF based on a longer linear ligand: electrochemical performance, reaction kinetics, and use as a novel anode material for sodium-ion batteries, Chem. Commun. 54 (2018) 11793–11796. doi:10.1039/C8CC06248J.

[43] Y. Park, D.-S. Shin, S.H. Woo, N.S. Choi, K.H. Shin, S.M. Oh, K.T. Lee, S.Y. Hong, Sodium Terephthalate as an Organic Anode Material for Sodium Ion Batteries, Adv. Mater. 24 (2012) 3562–3567. doi:10.1002/adma.201201205.

[44] D. Skoda, T. Kazda, L. Munster, B. Hanulikova, A. Styskalik, P. Eloy, D.P. Debecker, P. Vyroubal, L. Simonikova, I. Kuritka, Microwave-assisted synthesis of a manganese metal–organic framework and its transformation to porous MnO/carbon nanocomposite utilized as a shuttle suppressing layer in lithium–sulfur batteries, J. Mater. Sci. 54 (2019) 14102–14122. doi:10.1007/s10853-019-03871-4.

[45] W. Yang, X. Li, Y. Li, R. Zhu, H. Pang, Applications of Metal–Organic-Framework-Derived Carbon Materials, Adv. Mater. 1804740 (2018) 1804740. doi:10.1002/adma.201804740.

[46] Y.C. Wang, W.B. Li, L. Zhao, B.Q. Xu, MOF-derived binary mixed metal/metal oxide @carbon nanoporous materials and their novel supercapacitive performances, Phys. Chem. Chem. Phys. 18 (2016) 17941–17948. doi:10.1039/C6CP02374F.

[47] X. Li, C. Zeng, J. Jiang, L. Ai, Magnetic cobalt nanoparticles embedded in hierarchically porous nitrogen-doped carbon frameworks for highly efficient and well-recyclable catalysis, J. Mater. Chem. A. 4 (2016) 7476–7482. doi:10.1039/C6TA01054G.

[48] S. Dou, X. Li, L. Tao, J. Huo, S. Wang, Cobalt nanoparticle-embedded carbon nanotube/porous carbon hybrid derived from MOF-encapsulated Co 3 O 4 for oxygen electrocatalysis, Chem. Commun. 52 (2016) 9727–9730. doi:10.1039/C6CC05244D.

[49] X. Wan, R. Wu, J. Deng, Y. Nie, S. Chen, W. Ding, X. Huang, Z. Wei, A metal–organic framework derived 3D hierarchical Co/N-doped carbon nanotube/nanoparticle composite as an active electrocatalyst for oxygen reduction in alkaline electrolyte, J. Mater. Chem. A. (2018). doi:10.1039/C7TA10022A.

[50] G. Zou, H. Hou, P. Ge, Z. Huang, G. Zhao, D. Yin, X. Ji, Metal-Organic Framework-Derived Materials for Sodium Energy Storage, Small. 14 (2018) 1702648. doi:10.1002/smll.201702648.

[51] N. Ingersoll, Z. Karimi, D. Patel, R. Underwood, R. Warren, Metal organic framework-derived carbon structures for sodium-ion battery anodes, Electrochim. Acta. 297 (2019) 129–136. doi:10.1016/j.electacta.2018.11.140.

[52] M. Jacquemin, M.J. Genet, E.M. Gaigneaux, D.P. Debecker, Calibration of the X-Ray Photoelectron Spectroscopy Binding Energy Scale for the Characterization of Heterogeneous Catalysts: Is Everything Really under Control?, ChemPhysChem. 14 (2013) 3618–3626. doi:10.1002/cphc.201300411.

[53] D.A. Shirley, High-Resolution X-Ray Photoemission Spectrum of the Valence Bands of Gold, Phys. Rev. B. 5 (1972) 4709–4714. doi:10.1103/PhysRevB.5.4709.

[54] S. Lowell, J.E. Shields, M.A. Thomas, M. Thommes, Surface Area Analysis from the Langmuir and BET Theories, in: Charact. Porous Solids Powders Surf. Area, Pore Size Density, Springer Netherlands, 2004: pp. 58–81. doi:10.1007/978-1-4020-2303-3_5.

[55] J. Rouquerol, F. Rouquerol, P. Llewellyn, G. Maurin, K. Sing, Adsorption by Powders and Porous Solids Principles, Methodology and Applications, Academic Press, Amsterdam, 2014.

[56] Y.-J. Zhu, F. Chen, Microwave-Assisted Preparation of Inorganic Nanostructures in

Liquid Phase, Chem. Rev. 114 (2014) 6462–6555. doi:10.1021/cr400366s.

[57] K. Uemura, S. Kitagawa, M. Kondo, K. Fukui, R. Kitaura, H.C. Chang, T. Mizutani, Novel flexible frameworks of porous cobalt(II) coordination polymers that show selective guest adsorption based on the switching of hydrogen-bond pairs of amide groups, Chem. - A Eur. J. 8 (2002) 3586–3600. doi:10.1002/1521-3765(20020816)8:16<3586::AID-CHEM3586>3.0.CO;2-K.

[58] A.G. Nasibulin, E.I. Kauppinen, D.P. Brown, J.K. Jokiniemi, Nanoparticle Formation via Copper (II) Acetylacetonate Vapor Decomposition in the Presence of Hydrogen and Water, J. Phys. Chem. B. 105 (2001) 11067–11075. doi:10.1021/jp0114135.

[59] G.B. Deacon, R.J. Phillips, Relationships between the carbon-oxygen stretching frequencies of carboxylato complexes and the type of carboxylate coordination, Coord. Chem. Rev. 33 (1980) 227–250. doi:10.1016/S0010-8545(00)80455-5.

[60] L. Valenzano, B. Civalleri, S. Chavan, S. Bordiga, M.H. Nilsen, S. Jakobsen, K.P. Lillerud, C. Lamberti, Disclosing the complex structure of UiO-66 metal organic framework: A synergic combination of experiment and theory, Chem. Mater. 23 (2011) 1700–1718. doi:10.1021/cm1022882.

[61] K. Babić-Samardžija, S.P. Sovilj, N. Katsaros, Spectral assignments and molecular modeling of dinuclear cobalt(II) complexes with a bridged bidentate β-diketone and a cyclic octaamine ligand, J. Mol. Struct. 694 (2004) 165–171. doi:10.1016/j.molstruc.2004.03.016.

[62] A. Shastri, A.K. Das, S. Krishnakumar, P.J. Singh, B.N. Raja Sekhar, Spectroscopy of N , N -dimethylformamide in the VUV and IR regions: Experimental and computational studies, J. Chem. Phys. 147 (2017) 224305. doi:10.1063/1.5006126.

[63] J. Zhao, X. Quan, S. Chen, Y. Liu, H. Yu, Cobalt Nanoparticles Encapsulated in Porous Carbons Derived from Core–Shell ZIF67@ZIF8 as Efficient Electrocatalysts for Oxygen Evolution Reaction, ACS Appl. Mater. Interfaces. 9 (2017) 28685–28694. doi:10.1021/acsami.7b10138.

[64] N.R. Dhumal, M.P. Singh, J.A. Anderson, J. Kiefer, H.J. Kim, Molecular Interactions of a Cu-Based Metal–Organic Framework with a Confined Imidazolium-Based Ionic Liquid: A Combined Density Functional Theory and Experimental Vibrational Spectroscopy Study, J. Phys. Chem. C. 120 (2016) 3295–3304.

doi:10.1021/acs.jpcc.5b10123.

[65] L. Li, R. Jiang, W. Chu, H. Cang, H. Chen, J. Yan, Cobalt nanoparticles embedded in a porous carbon matrix as an efficient catalyst for ammonia decomposition, Catal. Sci. Technol. 7 (2017) 1363–1371. doi:10.1039/C7CY00086C.

[66] B. Rivas-Murias, V. Salgueiriño, Thermodynamic CoO-Co 3 O 4 crossover using Raman spectroscopy in magnetic octahedron-shaped nanocrystals, J. Raman Spectrosc. 48 (2017) 837–841. doi:10.1002/jrs.5129.

[67] R. He, S. Sucharitakul, Z. Ye, C. Keiser, T.E. Kidd, X.P.A. Gao, Laser induced oxidation and optical properties of stoichiometric and non-stoichiometric Bi2Te3 nanoplates, Nano Res. 8 (2015) 851–859. doi:10.1007/s12274-014-0567-z.

[68] G. Greczynski, L. Hultman, X-ray photoelectron spectroscopy: Towards reliable binding energy referencing, Prog. Mater. Sci. 107 (2020) 100591. doi:10.1016/j.pmatsci.2019.100591.

[69] M. Smith, L. Scudiero, J. Espinal, J.-S. McEwen, M. Garcia-Perez, Improving the deconvolution and interpretation of XPS spectra from chars by ab initio calculations, Carbon N. Y. 110 (2016) 155–171. doi:10.1016/j.carbon.2016.09.012.

[70] M.C. Biesinger, B.P. Payne, A.P. Grosvenor, L.W.M. Lau, A.R. Gerson, R.S.C. Smart, Resolving surface chemical states in XPS analysis of first row transition metals, oxides and hydroxides: Cr, Mn, Fe, Co and Ni, Appl. Surf. Sci. 257 (2011) 2717–2730. doi:10.1016/j.apsusc.2010.10.051.

[71] A. Song, W. Yang, W. Yang, G. Sun, X. Yin, L. Gao, Y. Wang, X. Qin, G. Shao, Facile Synthesis of Cobalt Nanoparticles Entirely Encapsulated in Slim Nitrogen-Doped Carbon Nanotubes as Oxygen Reduction Catalyst, ACS Sustain. Chem. Eng. 5 (2017) 3973–3981. doi:10.1021/acssuschemeng.6b03173.

[72] H. Niu, Q. Chen, H. Zhu, Y. Lin, X. Zhang, Magnetic field-induced growth and self-assembly of cobalt nanocrystallites, J. Mater. Chem. 13 (2003) 1803–1805. doi:10.1039/b303024e.

[73] K.-Y.A. Lin, Y.-C. Chen, C.-F. Huang, Magnetic carbon-supported cobalt prepared from one-step carbonization of hexacyanocobaltate as an efficient and recyclable catalyst for activating Oxone, Sep. Purif. Technol. 170 (2016) 173–182.

doi:10.1016/j.seppur.2016.06.048.

[74] K.Y. Andrew Lin, F.K. Hsu, W. Der Lee, Magnetic cobalt-graphene nanocomposite derived from self-assembly of MOFs with graphene oxide as an activator for peroxymonosulfate, J. Mater. Chem. A. 3 (2015) 9480–9490. doi:10.1039/c4ta06516f.

[75] Y. Garsany, K. Swider-Lyons, Kinetic Activity in Electrochemical Cells, in: Springer Handb. Electrochem. Energy, Springer Berlin Heidelberg, Berlin, Heidelberg, 2017: pp. 423–445. doi:10.1007/978-3-662-46657-5_14.

[76] V.G. Pol, E. Lee, D. Zhou, F. Dogan, J.M. Calderon-Moreno, C.S. Johnson, Spherical Carbon as a New High-Rate Anode for Sodium-ion Batteries, Electrochim. Acta. 127 (2014) 61–67. doi:10.1016/j.electacta.2014.01.132.

[77] N. Sun, H. Liu, B. Xu, Facile synthesis of high performance hard carbon anode materials for sodium ion batteries, J. Mater. Chem. A. 3 (2015) 20560–20566. doi:10.1039/C5TA05118E.

[78] Z. Li, L. Ma, T.W. Surta, C. Bommier, Z. Jian, Z. Xing, W.F. Stickle, M. Dolgos, K. Amine, J. Lu, T. Wu, X. Ji, High Capacity of Hard Carbon Anode in Na-Ion Batteries Unlocked by PO x Doping, ACS Energy Lett. 1 (2016) 395–401. doi:10.1021/acsenergylett.6b00172.

[79] S. Wenzel, T. Hara, J. Janek, P. Adelhelm, Room-temperature sodium-ion batteries: Improving the rate capability of carbon anode materials by templating strategies, Energy Environ. Sci. 4 (2011) 3342. doi:10.1039/c1ee01744f.

[80] T. Chen, L. Pan, T. Lu, C. Fu, D.H.C. Chua, Z. Sun, Fast synthesis of carbon microspheres via a microwave-assisted reaction for sodium ion batteries, J. Mater. Chem. A. 2 (2014) 1263–1267. doi:10.1039/C3TA14037G.